Geomorphology xxx (2012) xxx–xxx

Contents lists available at SciVerse ScienceDirect

Geomorphology

journal homepage: www.elsevier.com/locate/geomorph

Complex rupture mechanism and topography control symmetry of mass-wasting pattern, 2010 Haiti earthquake

Tolga Gorum [a,b,*], Cees J. van Westen [a], Oliver Korup [c], Mark van der Meijde [a], Xuanmei Fan [a,d], Freek D. van der Meer [a]

[a] Faculty of Geo-Information Science and Earth Observation (ITC), University of Twente, 7500 AE, Enschede, P.O. Box 217, The Netherlands
[b] Natural Sciences Research Center, Yildiz Technical University, Esenler, 34220 Istanbul, Turkey
[c] Institut für Erd- und Umweltwissenschaften, Universität Potsdam, D-14476 Potsdam, Germany
[d] The State Key Laboratory of Geohazards Prevention and Geoenvironment Protection (Chengdu University of Technology), Chengdu, Sichuan, China

ARTICLE INFO

Article history:
Received 16 August 2012
Received in revised form 26 November 2012
Accepted 29 November 2012
Available online xxxx

Keywords:
Landslide
Earthquake
Thrust fault
Fault rupture dynamics
Topography
Haiti

ABSTRACT

The 12 January 2010 M_w 7.0 Haiti earthquake occurred in a complex deformation zone at the boundary between the North American and Caribbean plates. Combined geodetic, geological and seismological data posited that surface deformation was driven by rupture on the Léogâne blind thrust fault, while part of the rupture occurred as deep lateral slip on the Enriquillo–Plantain Garden Fault (EPGF). The earthquake triggered >4490 landslides, mainly shallow, disrupted rock falls, debris-soil falls and slides, and a few lateral spreads, over an area of ~2150 km^2. The regional distribution of these slope failures defies those of most similar earthquake-triggered landslide episodes reported previously. Most of the coseismic landslides did not proliferate in the hanging wall of the main rupture, but clustered instead at the junction of the blind Léogâne and EPGF ruptures, where topographic relief and hillslope steepness are above average. Also, low-relief areas subjected to high coseismic uplift were prone to lesser hanging wall slope instability than previous studies would suggest. We argue that a combined effect of complex rupture dynamics and topography primarily control this previously rarely documented landslide pattern. Compared to recent thrust fault-earthquakes of similar magnitudes elsewhere, we conclude that lower static stress drop, mean fault displacement, and blind ruptures of the 2010 Haiti earthquake resulted in fewer, smaller, and more symmetrically distributed landslides than previous studies would suggest. Our findings caution against overly relying on across-the-board models of slope stability response to seismic ground shaking.

1. Introduction

The M_w 7.0 Haiti earthquake struck the southern part of Hispaniola Island at 16:53 local time (21:53 UTC) on 12 January 2010. It was the deadliest earthquake in South Hispaniola's recent history, with more than 316,000 fatalities; 300,000 people injured; 35,000 buildings destroyed; and 1.5 million people left homeless (Cavallo et al., 2010). The earthquake hypocenter was at 18.44° N, 72.57° W, at a depth of 13 km in a poorly seismic instrumented region. The U.S. Geological Survey (USGS) National Earthquake Information Center (NEIC) and the global centroid moment tensor solutions, associated the initial location and mechanism for this event with the rupture of the sinistral Enriquillo–Plantain Garden Fault (EPGF) zone, a major fault system accommodating 7 ± 2 mm year^{-1} of relative motion between the Caribbean plate and Gonâve microplate (Mann et al., 1984; Manaker et al., 2008; Hayes et al., 2010; Fig. 1).

The region most affected by the earthquake is located on the junction of the EPGF zone and the Transhaitian Belt (THB), which are the two major crustal structures in eastern Hispaniola (Fig. 1a and b). From historical records the EPGF was known to have caused $M>7$ earthquakes in the 18th century (Mann et al., 1995; Calais et al., 2010; Bakun et al., 2012). The 2010 earthquake, however, did not create any detectable surface rupture (Prentice et al., 2010; Mercier de Lépinay et al., 2011), raising the question of which fault was ultimately responsible. Studies that integrated the aftershock moment tensor solutions (Mercier de Lépinay et al., 2011), space geodetic measurements (Hayes et al., 2010; Hashimoto et al., 2011), and field-based uplift data revealed a complex rupture process involving slip on multiple faults (Hayes et al., 2010), with surface deformation driven by rupture on the N264° E north-dipping Léogâne blind thrust fault, and only minor deep sinistral slip along the EPGF. Fault model results show that the main seismogenic Léogâne blind thrust fault was responsible for ~80% of the seismic moment (Hayes et al., 2010). The direction of the rupture propagation mainly focused on S and SE, with increased amplitudes in the direction of rupture propagation, and decreased ground-motion in the backward direction due to source directivity (Hayes et al., 2010; Hough et al., 2010).

* Corresponding author at: Faculty of Geo-Information Science and Earth Observation (ITC), University of Twente, 7500 AE, Enschede, P.O. Box 217, The Netherlands. Tel.: +31 53 487 4504.
E-mail address: gorum@itc.nl (T. Gorum).

0169-555X/$ – see front matter © 2012 Elsevier B.V. All rights reserved.
http://dx.doi.org/10.1016/j.geomorph.2012.11.027

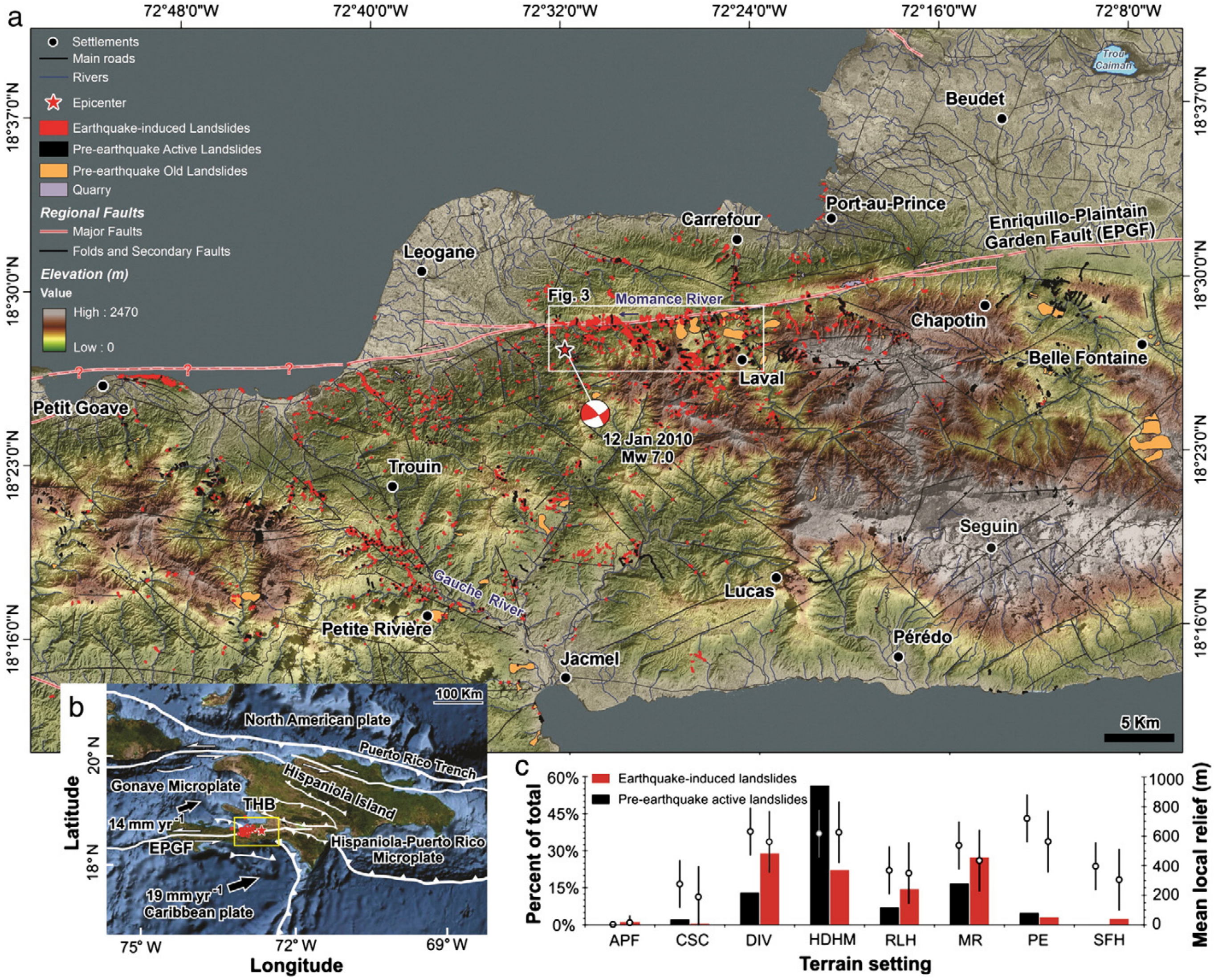

Fig. 1. Tectonic setting and landslide distribution map of the study area. (a) Area surrounding the M_w 7.0 January 2010 Haiti earthquake epicenter; beach ball shows focal mechanism (earthquake.usgs.gov). (b) Tectonic setting of the Caribbean plate boundaries. Red star and the points are locations of main shock and major aftershock distributions, respectively. (c) Topographic setting and mean local relief (white circles with $\pm 1\sigma$ whiskers) of pre- and post-earthquake landslides: alluvial plains and fans (APF), coastal cliff (CSC), deeply incised valley (DIV), dissected hilly and mountainous terrain (HDHM), round crested slopes and hills (RLH), moderately steep slopes (MR), plateau escarpments (PE), and steep faulted hills (SFH).

Integration of the geodetic and seismologic data further shows that some portion of the rupture occurred as deep lateral motion on a steeply (70°) south-dipping fault (Fig. 1b), i.e. the EPGF, in addition to slip on thrust faults to the north (Hayes et al., 2010; Mercier de Lépinay et al., 2011).

The 2010 earthquake not only caused severe loss of lives and infrastructure, but also triggered thousands of landslides (Fig. 1a). Here we explore the possible influence of complex fault slip, spatially variable vertical deformation, topography, and lithology on the regional distribution and abundance of coseismic slope failures. Our objective is to quantify from a detailed inventory of nearly 4500 post-earthquake landslides the potential contributions of seismic, topographic, and rock-type controls as documented by radar remote sensing, fault-geometry models, digital elevation data, and geological maps.

2. Study area

Our study focuses on the main epicentral area of the 2010 earthquake in central Haiti. The regional geology of Hispaniola is characterized by NW–SE oriented sub-parallel belts of igneous, metamorphic and sedimentary rocks (Sen et al., 1988; Escuder-Viruete et al., 2007). The basement in the North of the study area is largely composed of Cretaceous to Paleogene island arc rocks (Sen et al., 1988), covered by Neogene sediments and unconformable Quaternary alluvial deposits that record sustained tectonics since the late Pliocene (Mann et al., 1984; Fig. 2a). Eocene limestones are mainly exposed in the Momance River and in the SW of the study area: These rocks are pervasively fractured along the EPGF and Gauche River. The Cretaceous Dumisseau Formation features (pillow) basalts and minor picrites interlayered with pelagic limestones that crop out in the southern part of the study area, including the Massif de la Selle (Fig. 2a). The basalts are deeply weathered and have lateritic profiles. Sustained uplift and erosion delivered lateritic detritus from basaltic terrain into karst structures in the adjacent limestones (Bird et al., 1992).

The left-lateral EPGF is the most prominent strike-slip fault in the region, cutting across the Southern Peninsula of Haiti at N85°E. Two M_w 7.5 earthquakes have occurred in this fault zone on 21 November 1751, and 3 June 1770 (Mann et al., 1995; Bakun et al., 2012). In the study area, the highly linear segment of the EPGF coincides with the Momance River valley that runs parallel to the fault in an E–W direction, indicating a major tectonic control on topography. The topographic grain of NW–SE and E–W directed valley and ridge systems is consistent with regional principal stress axes. Mean elevation increases from north to south, rising up to ~2500 m a.s.l. on the plateau. Topographic relief is high in the southern EPGF, along the central Momance valley, and the north-facing slopes of Massif de la Selle, with distinctly steeper mean hillslope gradients (~0.53) compared to the average of the study area (~0.25).

Haiti's tropical climate features periodic droughts and tropical cyclones (hurricanes), and the precipitation pattern mirrors the N–S gradient in topographic relief. The area experiences two rainy seasons per year, from April to June and from October to November, and a hurricane season from early June until the end of November. The 2010 earthquake occurred in the dry season. Haiti suffered significant losses due to the 2004 tropical storm Jeanne, which caused heavy rainfall, massive flooding, and landslides in southern Hispaniola. Additionally, Hurricanes Fay, Gustav, Hanna, and Ike heavily affected the region in 2008 (NOAA, 2012).

3. Materials and methods

We mapped the locations and areas of individual landslides from pre- and post-earthquake high-resolution satellite images and aerial photos covering a total of ~7,000 km^2. The pre-earthquake images were high-resolution Worldview (0.5 m) and Quickbird (0.6 m), and panchromatic OrbView-3 (1 m) data. Post-earthquake images included GeoEye-1 (0.4-m) data and high-resolution Google® and Microsoft™ UltraCamG aerial photos (0.15 to 0.30 m) covering the most heavily affected region (see Supplementary Information Fig. S1 and Table S1). Satellite images and aerial photographs were geometrically corrected using 52 ground control points (GCPs) well distributed within the post-earthquake images that predated the orthorectified GeoEye-1 and Microsoft™ UltraCamG aerial photos. We used a polynomial nearest neighbor re-sampling method and the GCPs to establish a transformation model for producing georectified images. The average georectification accuracy has a root mean square error (*RMSE*) of <1 pixel. Overlays of pre- and post-earthquake images did not produce any visible mismatches. We mainly used images with cloud and shadow coverage of <0.4% of the study area.

Visual landslide detection was based on true-color composites and panchromatic images, using monoscopic image interpretation. To identify individual slope failures in the high-resolution images, we used diagnostic features such as differences in shape, size, color, tone, texture, and landform assemblages (van Zuidam, 1985; van Westen et al., 2008; Fiorucci et al., 2011; Gorum et al., 2011; Fan et al., 2012a,b). We further used oblique-aerial photos taken from helicopters shortly after the earthquake (US Geological Survey, 2010; http://cires.colorado.edu/~bilham). We mapped 4492 coseismic landslides in total, though consider this an underestimate given some noise between pre- and post-earthquake imagery, which precluded clear recognition of landslide areas <20 m^2. Assuming that landslides mapped from images predating the 2010 earthquake were triggered mainly by rainstorms, we distinguished aseismic from coseismic, i.e. post-2010, landslide inventories. We computed the spatial density [km^{-2}] and the fraction of area [%] affected by landslides within a moving window of 1-km radius using a Gaussian kernel density estimator. To quantify the net effect of the earthquake on the abundance of landslides, we computed a re-activation rate [%] based on the comparison of the pre-earthquake landslide areas with the extent of coseismic landslide areas.

In order to assess the role of topography and surface-rupture process on the distribution of coseismic landslides, we combined various terrain metrics with available data on lithology and the distribution of vertical coseismic deformation. Regional-scale coseismic deformation rate and rupture process of the earthquake are part of a detailed rupture model based on a joint inversion of interferometric synthetic aperture radar (InSAR), field based off-set measurements, and teleseismic body-wave data (Hayes et al., 2010). We computed hillslope gradient S_h from an ASTER Global Digital Elevation Model version 2 (GDEM-2) with a pixel resolution of 30 m using a best-fit plane in a 3×3 moving window. Local topographic relief H was computed from the same data as the maximum elevation range within a 1-km radius. We also computed a vector ruggedness measure (*VRM*) based on the dispersion of normal vectors of the terrain surface (Sappington et al., 2007) as a proxy of topographic response during the earthquake, incorporating variability in both slope aspect and gradient.

For exploring the potential effects of rock types on the occurrence of coseismic landslides, we digitized the scanned and orthorectified outlines of major tectonic structures and lithological units compiled by Lambert et al. (1987) at 1:250,000 scale. We derived density estimates of S_h for selected homogenous rock types in uplifted and subsided sections of the study area following the method of Korup (2008). The peaks of these distributions can be used as proxies for rock-mass strength at the regional scale (Korup, 2008; Korup and Schlunegger, 2009; Korup and Weidinger, 2011), and allow assessing the susceptibility of rock type to coseismic landsliding. We excluded areas of low coseismic landslide density (<0.01%) from this analysis. We plotted the coseismic deformation rate, landslide density, local relief and slope gradient along two swath profiles across the earthquake region, centered on the blind fault ruptures and the regions of maximum vertical coseismic deformation. Finally, we compiled inventories of coseismic landslides documented from recent reverse or thrust-faulting earthquakes that serve as a reference for linking fault geometries and rupture dynamics with regional patterns of coseismic landsliding.

4. Results

4.1. Regional landslide distribution

The 2010 Haiti earthquake triggered at least 4490 landslides over an area of ~2250 km^2, and up to a distance of ~46 km from the epicenter. The pre-2010 landslide inventory contains 22 potentially prehistoric and 1273 recently active landslides. The 2010 earthquake more than tripled the landslide abundance. Prehistoric, recent aseismic, coseismic landslides affected 19.4, 16.5 and 8 km^2, respectively. We find that 572 landslides were re-activated during the 2010 earthquake, affecting a total of 0.7 km^2, or <0.04% of the study area. Thus some 700 pre-existing aseismic landslides were not re-activated by the 2010 Haiti earthquake.

The majority of coseismic landslides clustered in a 5-km wide corridor around the junction of the blind ruptures of the Léogâne fault and EPGF zones (Fig. 3). Instead of focusing on the hanging wall, most failures largely affected hillslopes of the Momance River valley, mountainous areas in the southern part of the study area, and in the deeply incised valleys of the southern EPGF. Most coseismic landslides were shallow rock and debris falls, involving the top few meters of strongly fractured and weathered bedrock, regolith, and lateritic soil (Jibson and Harp, 2011). Bedrock failures occurred mainly in the Eocene and the Upper Miocene limestones (Fig. 2c). In contrast, most of the aseismic landslides were soil and debris landslides that clustered in the thick lateritic horizons of the deeply weathered basalts, especially in the southern parts close to the EPGF (Fig. 2a). Several lateral spreads occurred in artificial fills and unconsolidated Quaternary deposits in the Port-au-Prince and Léogâne coastal fan delta (Figs. 1a and 2a). Landslides were also abundant in the higher parts of the Gauche River valley that follows a major NW–SE plunging fold axis overlaying strongly fractured Upper-Miocene limestones (Figs. 1a, 2a); one third of the coseismic landslides in this valley were re-activated failures. About 85% of both aseismic and coseismic landslides occurred in the SW facing valley slopes of Gauche River valley.

The dominant orientation of the coseismic landslides is consistent with the principal direction of neotectonic compression in the region. The landslide distribution in the uplifted section north of the fault and in the subsided southern section changes with major tectonic structures

Please cite this article as: Gorum, T., et al., Complex rupture mechanism and topography control symmetry of mass-wasting pattern, 2010 Haiti earthquake, Geomorphology (2012), http://dx.doi.org/10.1016/j.geomorph.2012.11.027

(Fig. 2b). Dominant neotectonic and topographic structures have E–W and NW–SE orientations, with narrow, deeply eroded valleys and steep mountain slopes containing >60% of the coseismic landslides; >80% of the landslides in these areas involved bedrock. In contrast, the orientation of the aseismic landslides is independent of the region's principal stress axes (Fig. 2b), with >55% occurring in densely dissected hilly to mountainous terrain (Fig. 1c).

The spatial abundance of coseismic landslides is high in the Momance River valley and up to ~5 km beyond to the south (Fig. 4a). Aseismic and coseismic landslide density varies from north to south,

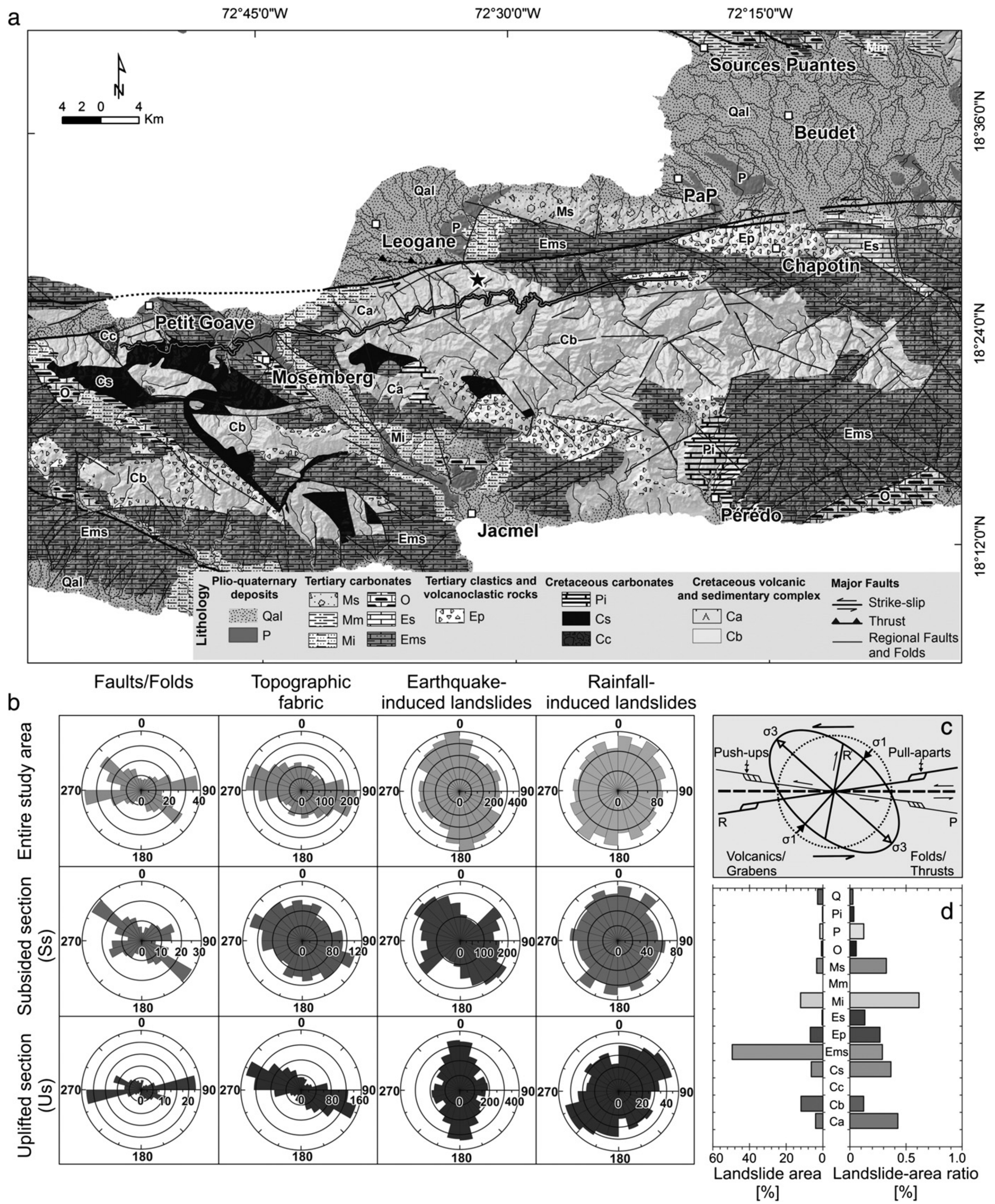

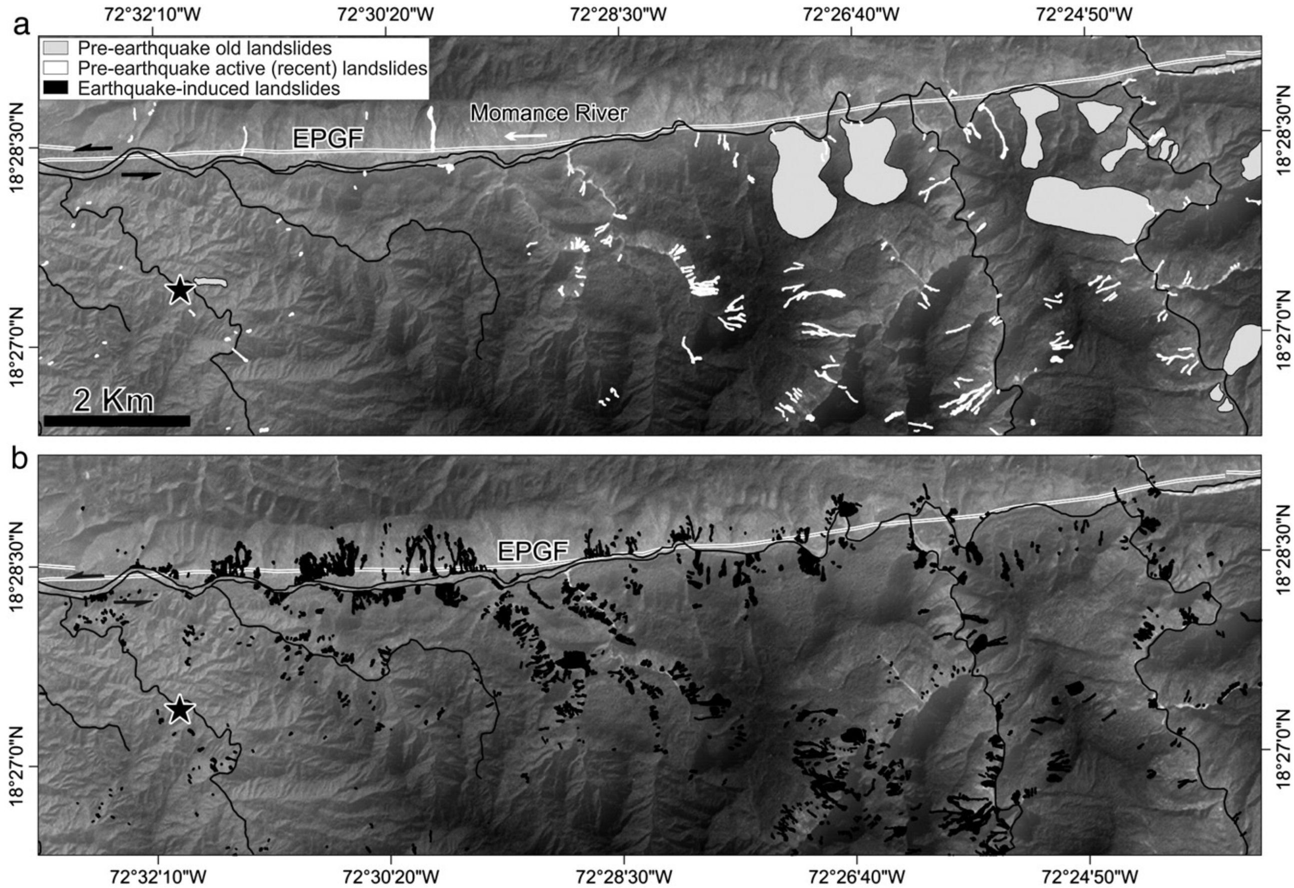

Fig. 3. Distribution of (a) coseismic and (b) aseismic landslides along a reach of the Momance River, Haiti; black star is location of 2010 earthquake epicenter; white arrow is flow direction. Old landslides may likely be of prehistoric origin.

with a minimum in the SW plateau, where seismic re-activation was low (Fig. 4).

Much higher landslide densities occur in the north of the EPGF, but decrease dramatically in the eastern extension of the fault (~72.18° N). In the south, except for the upper section of the Gauche valley, and in the east, the peaks of aseismic landslide abundance are more randomly distributed compared to those of the coseismic slope failures (Fig. 4a, b). A swath profile across the south-central part of Haiti underlines these gradients in aseismic and coseismic landslide density and re-activation rate (Fig. 4d–g). In the low-gradient deltas, coseismic landslides affected 0.2% to 5% of the area. Coseismic landsliding rates increase to 5% on steeper slopes of the Momance valley, where maximum aseismic landsliding rates are up to 2% (Fig. 4d, e). Nearly 40% of the total coseismic landslides occurred in these valley slopes, including the largest slope failures along the Momance River up to the eastern termination of the blind ruptures of the Léogâne and EPGF (Fig. 4b, e). Further south, the area near the boundary between uplifted and subsided sections has the highest re-activation rates. Re-activated landslide numbers and the rate of re-activation gradually decrease from >95 km^{-2}, and 0.5% to <65 km^{-2}, and 0.2% towards to the south, respectively (Fig. 4f, g). Despite this decrease, re-activation rates increase again with a distinct peak in the upper catchment the Gauche River (18.18°–18.22° N, Fig. 4f, g).

4.2. Coseismic deformation and fault rupture geometry

The complex rupture of the 2010 earthquake generated two major deformation areas: the first is the uplifted section that covers a corridor 5 km south of the EPGF zone up to the alluvial fan deltas in the north; and the second is along a subsided section covering the mountainous areas to the south (Fig. 5a). Vertical deformation ranged from −0.6 to +0.6 m (Hayes et al., 2010), with most coseismic landslides clustering in areas with +0.01 to +0.3 m offsets (Fig. 5). Landslide abundance shows no clear relationship with vertical deformation rate. For example, the number of landslides, mainly lateral spreads and shallow debris falls and slides, in coastal parts of the Léogâne fan delta is limited despite the high coseismic vertical offsets of up to +0.6 m (Fig. 5a, b). These offsets are three times higher than those in the peak areas of landsliding east of the epicenter. Visual inspection shows that clustering of coseismic landslides spatially coincides with the coseismic fault geometries. Landslide abundance in the high-elevation southern slopes of the EPGF is bracketed by the up- and down-dip edges of the

Fig. 2. Geological setting of the study area. (a) Geologic map of the study area (after Lamber et al., 1987). Qal: Quaternary alluvium, P: Pliocene weakly cemented sandstones, marls, and clastic deposits, Ms: Late Miocene limestone, marls, and sandstone, Mm: Middle Miocene blue-grey marls and neritic limestone, Mi: Early Miocene flysch and limestone, O: Oligocene chalk and marly limestone, Es: Late Miocene pelagic limestone, Ems: Middle to Late Miocene limestone, Ep: Late Paleocene–Early to Middle Eocene conglomerates, sandstone and volcanoclastics (Massif de la Selle), Cs: Senonian pelagic limestone, Pi: Cretaceous marls and marly limestone, Cc: Cretaceous limestone interlayered with reddish marls, Ca: Cretaceous volcanic and altered volcanic rocks, intermediate lava and pyroclastic rocks, and Cb: Cretaceous tholeiitic and sedimentary complex (fm. Dumisseau) pillowed and massive basalts and minor picrites interlayered with pelagic limestones. White thick line is vertical deformation signal from InSAR (Hayes et al., 2010) delimiting boundary between uplifted northern and subsided southern parts of earthquake-affected region. (b) Rose diagrams of faults and folds, topographic fabric, and runout directions of the co- and aseismic landslides in the entire study area, and the subsided and uplifted parts, respectively. (c) Strain ellipse of structures predicted in a left-lateral strike-slip plate boundary zone with east–west relative plate motion (after Mann et al., 1984). (d) Landslide area and landslide-area ratio for each geological unit.

Please cite this article as: Gorum, T., et al., Complex rupture mechanism and topography control symmetry of mass-wasting pattern, 2010 Haiti earthquake, Geomorphology (2012), http://dx.doi.org/10.1016/j.geomorph.2012.11.027

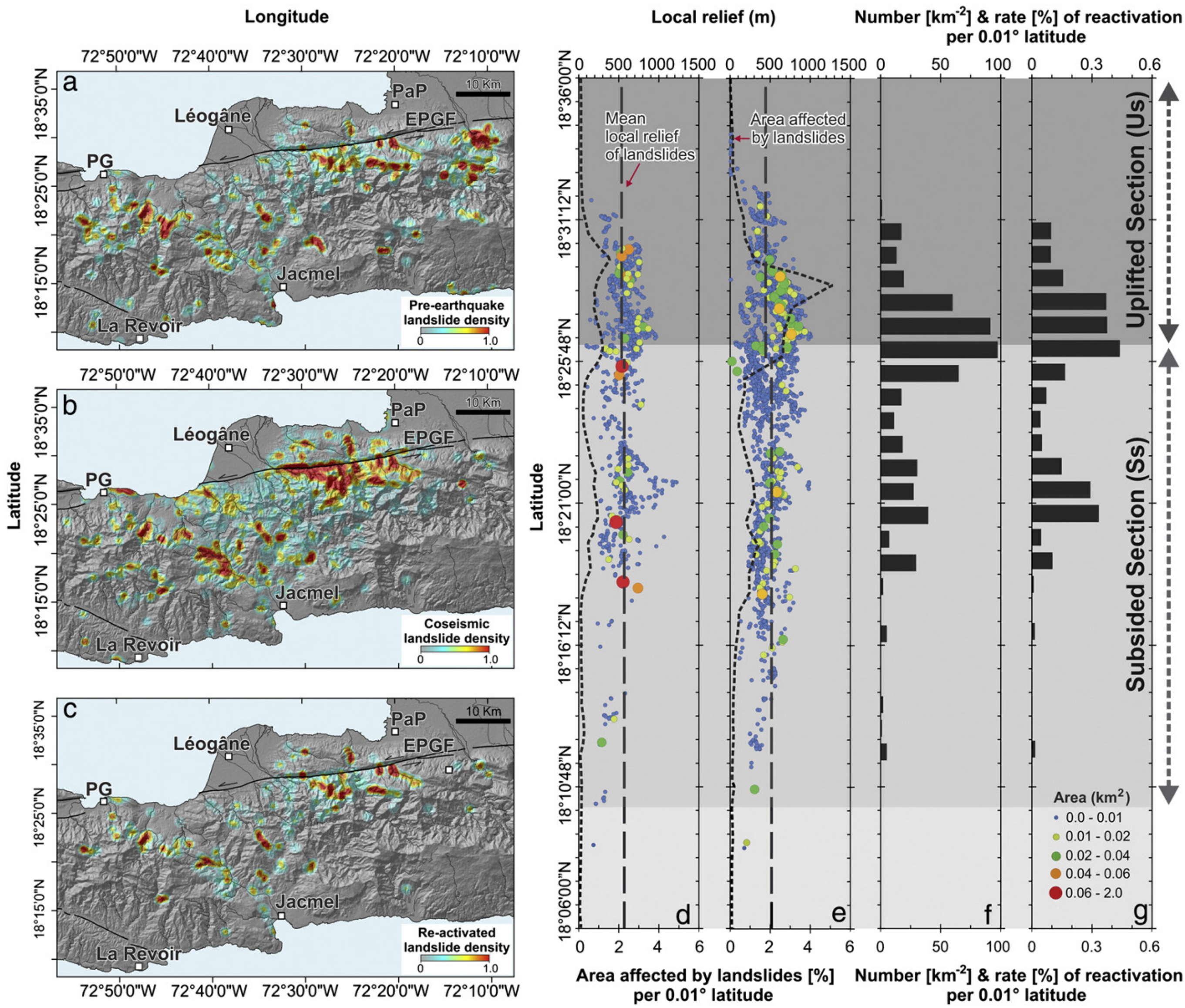

Fig. 4. Regional distribution of co- and aseismic landslides, and re-activated slope failures. (a) Normalized spatial density of pre-earthquake aseismic landslides within 1-km radius (see text). (b) Spatial density of coseismic landslides. (c) Spatial density of re-activated landslides. (d and e) Fraction of area affected by (d) aseismic and (e) coseismic landslides per 0.01° latitude; circles are individual landslide locations scaled by area (see legend in panel g). Thin black dashed lines are areas affected by the landslides; thick black dashed lines are mean local relief of coseismically uplifted and subsided areas. (f and g) Histograms of (f) point density [km^{-2}] and (g) rate [%] of re-activated landslides for 0.01° latitude bins; PaP: Port-au-Prince; PG: Petit Goave.

coseismic rupture (Fig. 5c, d). Coseismic landslide occurrence in the S and SW of the epicenter is consistent with the direction of rupture propagation (directivity), indicating that the dominant southward direction of coseismic slip could have caused increasing ground-motion amplitudes southward.

4.3. Hillslope steepness and rock-type effects

Density estimates of hillslope gradients for four paired sample regions of homogeneous lithologies in which the majority of coseismic landslides occurred shows that different rocks have differing modal hillslope inclinations. These modes are not uniform across the uplifted and subsided sections (Fig. 6a, b). Hillslope gradients of the rocks in the subsided section (Ss), except for the Miocene limestone (Ems), have higher modes than the homogenous counterparts in the uplifted section (Us; Fig. 6a, b). Cretaceous volcanic rocks (Ca) and Early Miocene flysch and limestones (Mi) have modes at S_h ~0.35, and ~0.32, which are substantially below those of the Cretaceous tholeiitic–sedimentary complex (Cb), and Miocene limestone (Ems) in both sections of the blind ruptures (Fig. 6a, b), i.e. S_h ~0.42 and ~0.52, respectively.

Many of the coseismic landslides in *Ca* are clustered in the altered parts of the volcanic rocks, occurring at the base of slopes in the form of shallow soil landslides (Fig. 6a, b). On the other hand, Early Miocene flysch and limestones (Mi) sustain mainly bedrock landslides and the coseismic landslides in the subsided section occur in distinctly steeper slopes than their nearby (<10 km) counterparts in the uplifted sections in terms of both mean and modal slope gradients.

When comparing rock types in the uplifted and subsided sections, the steepest slope gradients occur in the Ems unit in the uplifted section (north), which also contains 45% of all coseismic landslides. Except for this unit, the slope gradients of coseismic landslides are generally higher in the rocks of the subsided section where coseismic landslides are considerably close to upper slopes and ridges crests.

The vector ruggedness measure (*VRM*) of individual landslides is high in the subsided section and where deformation is between 0.01 and 0.1 m, along the Momance River in the uplifted section. The lowest *VRM* occurs mostly in the northern part of the uplifted section. We also

Please cite this article as: Gorum, T., et al., Complex rupture mechanism and topography control symmetry of mass-wasting pattern, 2010 Haiti earthquake, Geomorphology (2012), http://dx.doi.org/10.1016/j.geomorph.2012.11.027

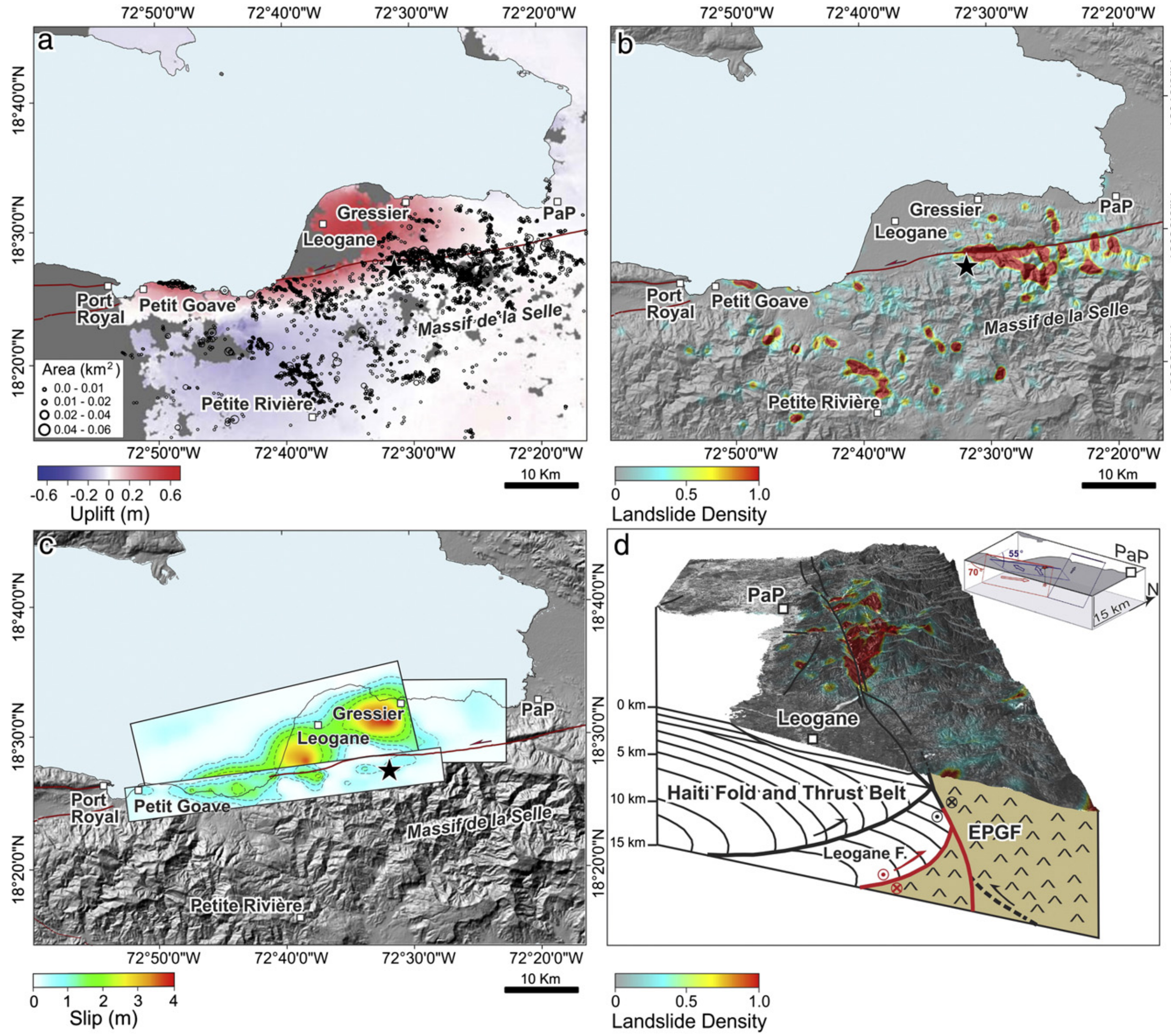

Fig. 5. Distribution of coseismic deformation, slip, and landslide density. (a) Vertical-deformation signal from InSAR (after Hayes et al., 2010); black circles are mapped coseismic landslides; the black star is the epicenter. (b) Normalized landslide density map (cf. Fig. 4). (c) Rupture model and coseismic slip amplitudes from inversion of InSAR data, field based off-set measurements, and broadband teleseismic body-waveform data (after Hayes et al., 2010). (d) Block diagram of the Léogâne thrust and Enriquillo–Plantain Garden Fault blind rupture. Normalized landslide density superimposed on data by Mercier de Lépinay et al. (2011). Inset block diagram shows proposed fault geometry by Hayes et al., (2010) for Haiti earthquake ruptures. Thick solid lines are surface projections of each fault; PaP: Port-au-Prince.

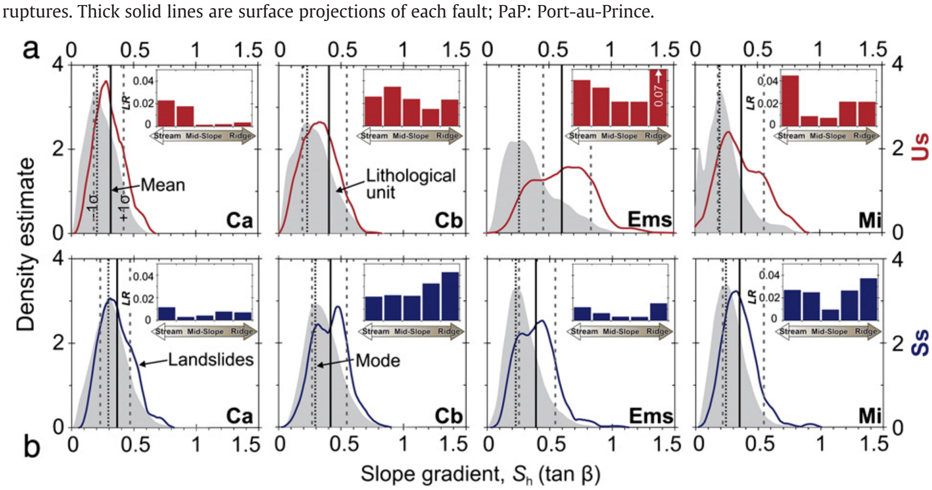

Fig. 6. Gaussian kernel density estimates of hillslope gradient in selected homogenous rock types in areas affected by coseismic (a) uplift (US), and (b) subsidence (SS). Samples are from 30-m ASTER DEM within 1 km radius, exclusive of low-gradient valley fills. Grey shades are hillslope gradients; thick lines are hillslope portions affected by landslides. Inset histograms show topographic position of coseismic landslides per rock type. Histograms bars (from left to right) are streams, lower, mid-, and upper slopes, and ridge crests derived from topographic position index (Jenness, 2006). Landslide ratio (*LR*) is fraction of area affected by landslides per rock type.

Please cite this article as: Gorum, T., et al., Complex rupture mechanism and topography control symmetry of mass-wasting pattern, 2010 Haiti earthquake, Geomorphology (2012), http://dx.doi.org/10.1016/j.geomorph.2012.11.027

find that the mean *VRM* of individual coseismic landslides in the subsided as well as the southern part of the uplifted sections exceeds the overall mean *VRM* of the earthquake struck region by a factor of ~2.5 (Fig. 7a, b).

5. Discussion

5.1. Combined effect of complex rupture mechanism and topography

Coseismic landslide abundance varies strongly with topographic relief and coseismic deformation in the study area. The W–E swath profile highlights the spatial coincidence of peaks in coseismic landslide abundance with the highest relief and steepest hillslopes in the uplifted section (Fig. 8a, Section 3 (S3)), hosting >80% of the mapped coseismic landslides. Although still observed in this section, coseismic deformation was below average. While the delta and low hilly zone in the west (Fig. 8a (S2)) were subjected to the highest coseismic deformation, the below-average local relief and hillslope gradients dampened coseismic landslide density, which strikingly mimics the trends of mean local relief and slope gradient over >70 km (Fig. 8c, d). The abrupt decrease in landslide density coincides with the lowest deformation at the eastern termination of the blind ruptures (Fig. 8a). From this point eastward, landslide density values increase slightly, with a significant fraction of re-activated slope failures (Fig. 8b). Although mean local relief in the terrain where aseismic landslides occur is higher than in areas affected by coseismic landslides, the reason for the clustered occurrence of coseismic landslides in the deeply incised valleys may be due to topographic amplification.

The N–S swath profile affords a more explicit picture of the combined effect of fault ruptures and topography on the coseismic landslide pattern, with 55% of the coseismic landslides located in the uplifted section (Fig. 8e, f). The lowest coseismic landslide density is in the northern part of the uplifted section despite high coseismic uplift rates, due to the low relief. The peak values of the coseismic landslide densities in the uplift section are in the southern part of the blind ruptures (Fig. 8e, f, Uplifted section 1 (Us1)). Most prominent in this section with few landslides are the below-average local relief and slope gradients. Areas with high landslide abundance in the 8-km narrow zone of the uplifted section had higher (or comparable) mean coseismic deformation, local relief and the slope gradient values compared to the overall mean (Fig. 8e–h). The spatial distribution of the landslide density in the subsided section differs from the uplifted section in terms of having lower density of landslides and more disperse distribution.

Despite the high values of mean local relief and slope steepness we infer that subdued landslide density peaks and the disperse distribution of the landslides are linked to first order with comparatively low rates of the coseismic deformation in the subsided section, which was relatively stationary and acted as a passive block during the earthquake. The earthquake also radiated some energy towards the southern part and the area affected by the landslides is nearly equal (i.e. 3.95 km^2) to that of the uplifted section. This nearly equal proportion is at odds with the area proportions of landslides triggered by thrust earthquakes reported previously.

The topographic response of the rugged terrain during the earthquake also differed in the uplifted and subsided sections (Fig. 7), likely because of seismic site effects. Coseismic landslides tend to preferentially occur on hillslopes inclined slightly steeper than the modal slope gradient, a finding that has been confirmed in many landslide-prone mountain ranges such as the United States (Wolinsky and Pratson, 2005), New Zealand (Korup, 2008), the Swiss Alps (Korup and Schlunegger, 2009), or Japan (Iwahashi et al., 2001, 2003). Topography can further change peak ground accelerations (*PGA*) values by ±50% in rugged terrains such as deeply incised valleys, ridges, steep slopes and cliffs (Faccioli et al., 2002; Paolucci, 2002; Meunier et al., 2008; Shafique et al., 2011). Judging from their topographic location (Fig. 6), terrain roughness and structural characteristics (Figs. 2b and 7), we infer that seismic site effects were prevalent in the subsided and southern part of the uplifted sections. Yet this cannot be directly shown with the seismic data because Haiti is a poorly seismic instrumented region. The coseismic landsliding rate with respect to topography differs in the deeply incised valleys and hilly terrains. In the Momance and Gauche River basins, coseismic landsliding rate is high and preferably attacking ridges and upper slopes. However, this pattern is not evident in many parts of the uplifted section (Fig. 6a).

5.2. Comparison with other thrust-faulting earthquakes

For a given magnitude, reverse and thrust-faulting earthquakes produce higher ground motion than strike-slip or normal-faulting earthquakes (Campbell, 1981; Oglesby et al., 1998, 2000). Also, hanging walls of reverse or thrust faults generally have a higher peak ground acceleration (*PGA*; Abrahamson and Somerville, 1996; Abrahamson and Silva,

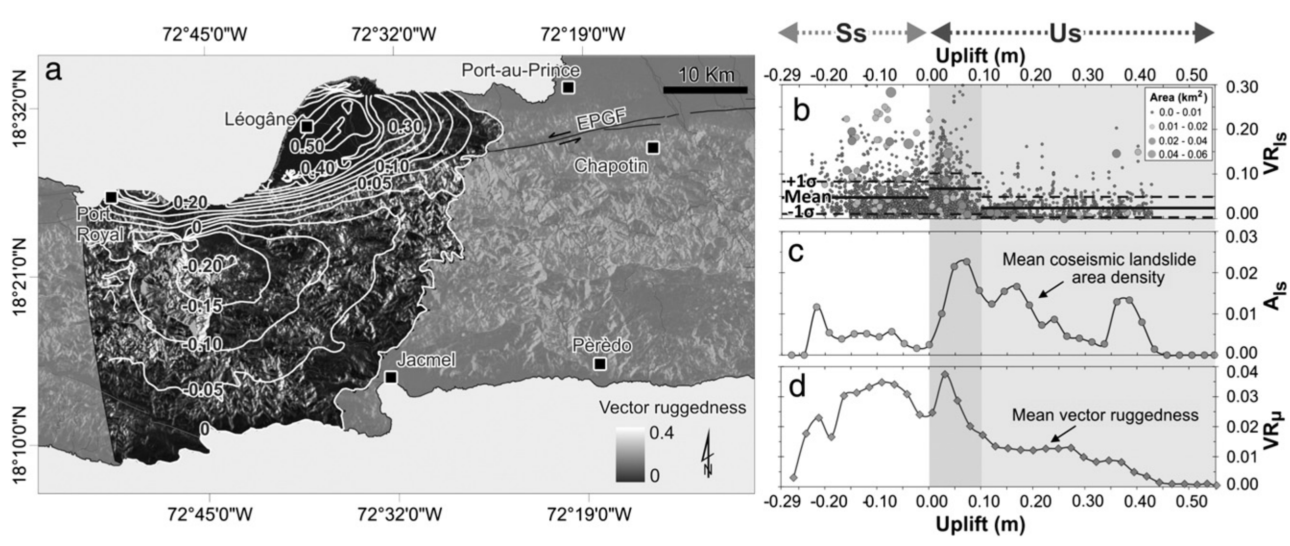

Fig. 7. Terrain roughness of coseismic landslides in relation to coseismic uplifts in epicentral region. (a) Vector ruggedness map displayed in grey tones with positive (uplift) and negative (subsidence) contour lines extracted from vertical-deformation signals of InSAR based on the range of high signal/noise (S/N) ratio (Hayes et al., 2010). (b) Vector ruggedness measure (*VRM*) values of individual landslides. (c) Mean coseismic landslide area density as a function of coseismic uplift. (d) Mean vector ruggedness variations. Black thick and dashed lines are means and $\pm 1\ \sigma$, respectively, circle size and color scaled by landslide area.

Please cite this article as: Gorum, T., et al., Complex rupture mechanism and topography control symmetry of mass-wasting pattern, 2010 Haiti earthquake, Geomorphology (2012), http://dx.doi.org/10.1016/j.geomorph.2012.11.027

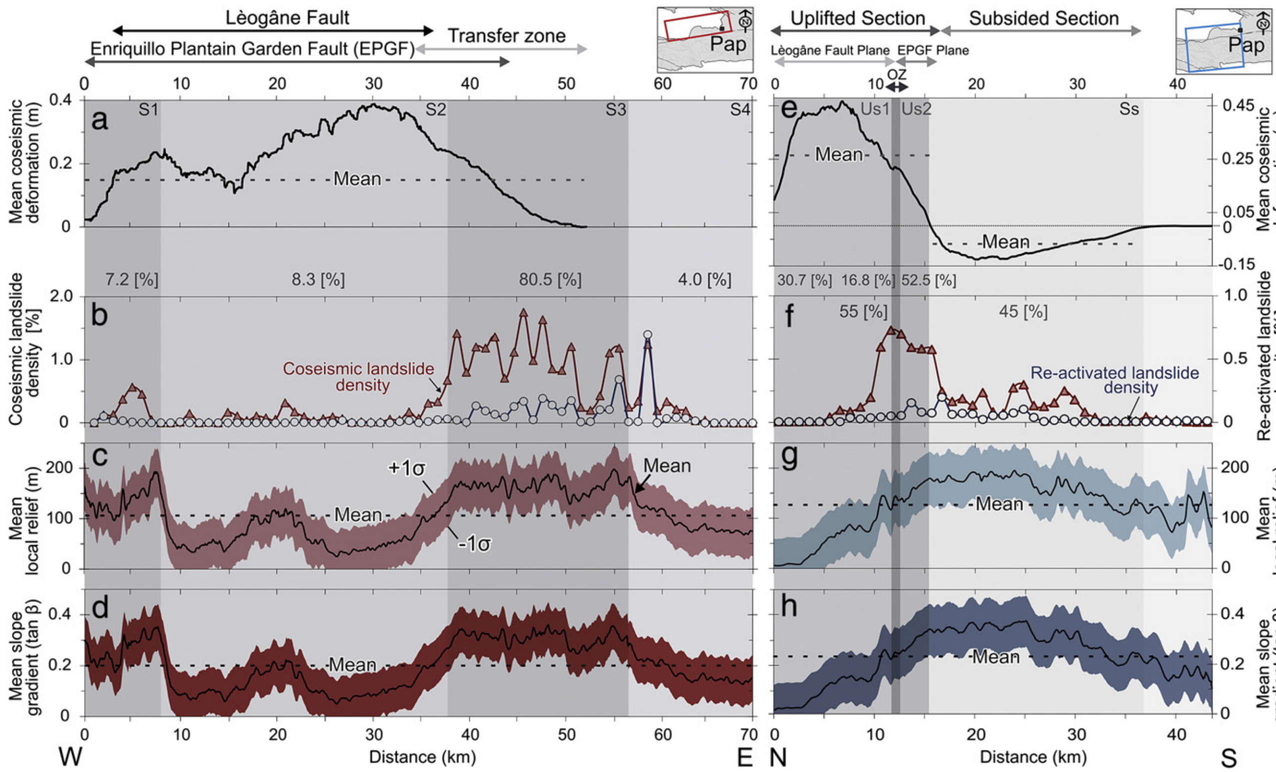

Fig. 8. Along-strike (W–E) distribution of (a) mean coseismic deformation (Hayes et al., 2010), (b) coseismic and re-activated normalized landslide density, (c) mean local relief, and (d) mean hillslope gradient in the uplifted section. N–S distribution of (e) mean coseismic deformation (Hayes et al., 2010), (f) coseismic and re-activated landslide density, (g) mean local relief, and (h) mean hillslope gradient in both uplifted and subsided parts. Inset maps show locations of the swaths. Black lines (c, d, g and h) and shadings are means and $\pm 1\ \sigma$ in 60-m bins. Light and dark grey boxes delimit peaks in normalized landslide density (b), and sub-sections of differing dominant fault geometries in (e). Dashed grey lines are regional means; scale differs between panels (b and f) in coseismic and re-activated landslide density.

1997). Campbell (2003) attributed this hanging-wall effect to a combination of radiation pattern, source directivity, and trapping of seismic waves within the hanging-wall wedge of the fault. This type of faulting may further enhance erosion rates because of elevated hanging walls through a gain in potential energy (Molnar et al., 2007), and reduced rock-mass strength from repeated seismic hanging-wall shattering (Korup, 2004).

Distinct asymmetric hanging-wall clustering of landslides triggered by thrust earthquakes supports this notion (Fig. 9). Inventories demonstrate the preponderance of coseismic landslides in the hanging

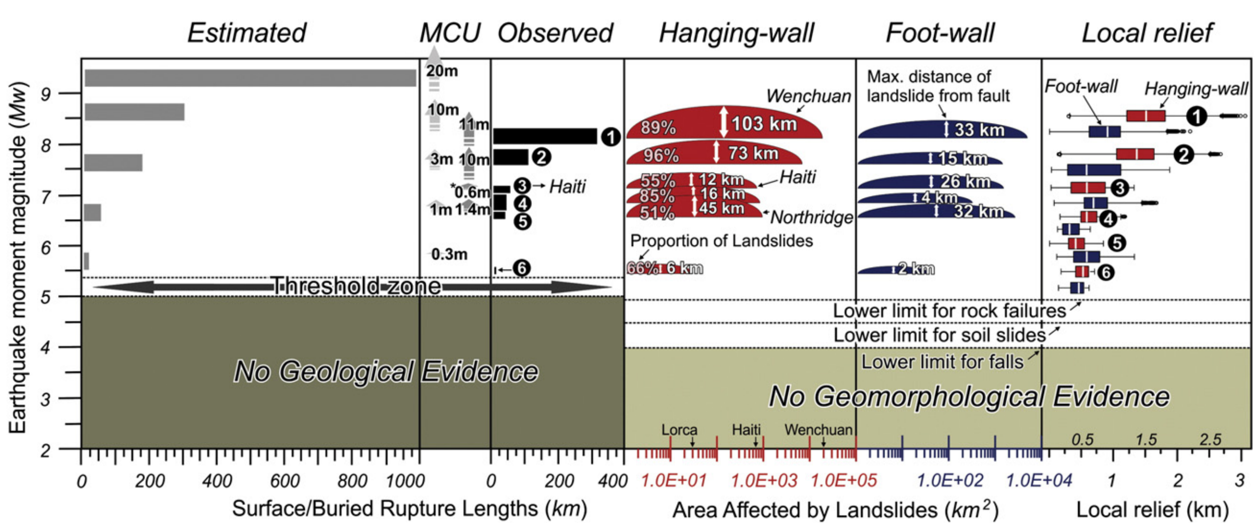

Fig. 9. Summary of coseismic landslide inventory data from documented reverse or thrust-fault earthquakes. Left panel shows extent of faulting recorded in historical (grey bars) and recent earthquakes (black bars; modified after McCalpin, 2009). Thick and thin black bars are lengths of surface and blind fault ruptures; estimates of surface rupture lengths (grey bars) and maximum coseismic uplift (light grey arrows) from Wells and Coppersmith (1994); lower limits from Bonilla (1988). Maximum coseismic uplift (*MCU*, dark grey arrows) and surface/blind ruptures: (1) Wenchuan, China, M_w 7.9 (Liu-Zeng et al., 2009); (2) Chi-Chi, Taiwan, M_w 7.6 (Chen et al., 2003); (3) Haiti *Mw* 7.0 (Hayes et al., 2010); (4) Iwate-Miyagi, Japan, M_w 6.9 (Ohta et al., 2008); (5) Northridge, USA, M_w 6.7 (Shen et al., 1996); and (6) Lorca, Spain, M_w 5.2 (Martinez-Diaz et al., 2012). Right panel shows hanging wall and foot-wall areas affected by coseismic landsliding, and box-and-whisker plots of local relief. Box delimits lower and upper quartiles and median; whiskers are 5th and 95th percentiles; open circles are outliers. Landslide inventory data from Gorum et al. (2011), Liao and Lee (2000), Yagi et al. (2009), Harp and Jibson (1995), and Alfaro et al. (2012); landslide lower limits are from Keefer (1984).

wall for the 1999 Chi-chi, Taiwan (M_w 7.6), the 2008 Wenchuan, China (M_w 7.9), and the 2008 Iwate-Miyagi Nairiku, Japan (M_w 6.9) earthquakes (Liao and Lee, 2000; Yagi et al., 2009; Gorum et al., 2011). However, landslides triggered by the 1994 Northrigde (M_w 6.7), and 2010 Haiti (M_w 7.0) earthquakes were nearly symmetrically distributed about the seismogenic fault (Fig. 9). The 2010 Haiti earthquake also differs from other thrust earthquakes of comparable magnitude because of its blind rupture. The event is similar to the 1994 Northridge earthquake (M_w 6.7)—which was also a blind rupture, though triggered 11,000 landslides — in terms of the ratio of coseismic hanging-wall to foot-wall landslides. The peculiar abundance of landslides triggered by the 1994 Northridge earthquake, given its magnitude, may be explained by the unusual large ground motions that indicated higher-than-average dynamic stress drops (Shen et al., 1996). Overall, we find that the ratio of coseismic hanging-wall to foot-wall landslides is lower in blind rupture earthquakes than in surface-rupture earthquakes (Fig. 9).

This finding awaits further confirmation from future earthquake-triggered landslide events. However, the attenuation relation for PGA on rock-site conditions considering the hanging wall scaling, shows a step in the ground motion from the hanging wall to the foot wall for surface-rupture earthquakes (Abrahamson and Silva, 2008). The difference in ground motion between hanging walls and foot walls is more pronounced for surface rupture-earthquakes, with the ground motion focusing on the hanging wall. For the case of blind-rupture earthquakes the transition of the ground motion proportion between the hanging wall and the foot wall is smooth, although the ground motion ratio remains higher on the hanging wall (Abrahamson and Silva, 2008). Short-period ground motions observed during blind-rupture earthquakes correspond to higher-than-average dynamic stress drops (Campbell, 2003), possibly due to a lack of surface rupture (Somerville, 2000; Somerville and Pitarka, 2006) or small total fault slip (Anderson, 2003).

During surface-rupture earthquakes the seismic energy focuses more to the surface, and significant increase in the static stress drop in terms of mean displacement may cause more coseismic landslides near the fault. Additionally, shear stress increases near the coseismic fault during surface-rupture earthquakes, depending on the width of the deformation zone and the coseismic slip amplitude (King et al., 1994; Harris, 1998; Stein, 1999). This may not only cause very large coseismic landslides in the hanging wall in a wide corridor (~8 km) along surface-rupturing faults. It also elevates the fraction of the area affected by slope failures up to six times higher compared to other sections (Liao and Lee, 2000; Gorum et al., 2011). Yet the most abundant size of landslides triggered by the 2010 earthquake is below those triggered by other surface-rupture earthquakes (Fig. 10).

Comparing landslide inventories of reverse or thrust-fault earthquakes with regard to potential controls of magnitude, occurrence of surface ruptures, and local relief, on mass-wasting response shows that seemingly minute differences do matter (Fig. 9). The number of coseismic landslides appears to be mainly controlled by earthquake magnitude rather than by whether the rupture breaks the surface or not. Yet mass-wasting reponses to earthquakes of similar magnitudes differ significantly. For example, the 2008 Iwate-Miyagi Nairiku, Japan (M_w 6.9) earthquake had a lower magnitude and affected areas of lower relief compared to the 2010 Haiti (M_w 7.0) event, though the hanging-wall effect was more pronounced and the landslides were larger in general (Figs. 9 and 10). Additionally, the hanging wall of the blind thrust-earthquakes are morphologically less expressed than those of the surface rupture-earthquakes, which may reflect that they are either recently established faults or simply older faults with rates of fault growth being outpaced by rates of erosion (Fig. 9).

Overall, different coseismic mass-wasting responses may be driven not only by magnitude, but also blind faulting, and low hanging-wall relief. Studies on earthquake-triggered landslides have so far largely neglected potential controls of fault geometry and rupture in this context. We surmise that the abundance, distribution pattern and size of coseismic landslides differ between blind and surface-rupturing earthquakes. Our study of the 2010 Haiti earthquake shows that this, together with the regional differences in geomorphology and tectonic setting, is essential in governing the pattern of coseismic landslides. Likewise, we find that the hillslope location of coseismic landslides is variable, and divergent from the pattern documented from previous earthquakes (Meunier et al., 2008).

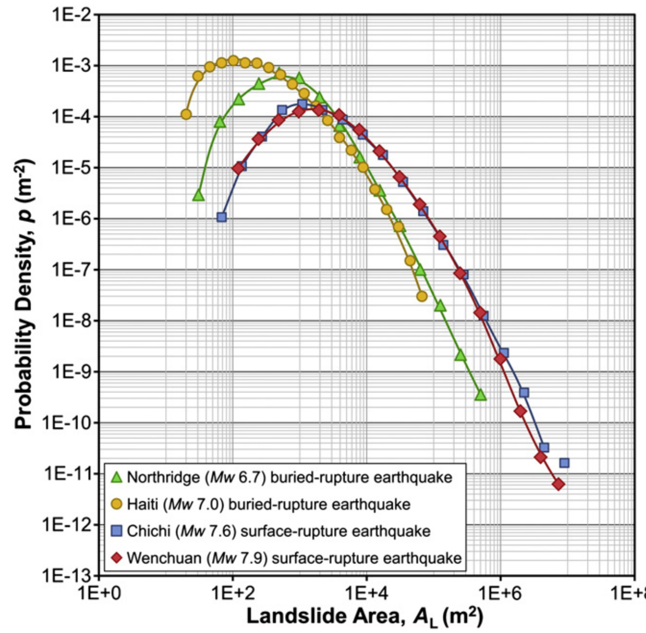

Fig. 10. Probability density of log-binned landslide deposit areas for blind and surface rupture-earthquakes (M_w 7.9 Wenchuan, China, 2008; M_w 7.6 Chi-Chi, Taiwan, 1999; M_w 7.0 Haiti, 2010; and M_w 6.7 Northridge, USA, 1994).

6. Conclusion

We show that the abundance, spatial pattern, and size distribution of coseismic landslides differ between blind and surface-rupturing earthquakes. Our study of the 2010 Haiti (M_w 7.0) earthquake shows that this, together with regional differences in topography and tectonic setting, is essential in governing the pattern of coseismic landslides. The earthquake triggered nearly 4500 landslides; 55% of these were located within the area uplifted during the earthquake. Distinct clusters of slope failures coincided with areas of extreme local relief and hillslope gradients. This pattern corroborates the notion that landslide-density changes mimic variations in coseismic deformation together with high topographic relief in the uplifted section. In contrast, landslides are more disperse in coseismic subsidence areas where topography is high, although the total landslide-affected area differs little. This is mainly due to low deformation and the limitation of slope failures to areas of varying topographic roughness and hillslope steepness. Landslide re-activation played an important role in this subsided section, and helps to gauge better the net coseismic landslide production. The absence of coseismic landslides in the high-relief southwestern parts indicates that the distribution of seismic energy is limited, also given that numerous pre-earthquake active landslides in this area were not re-activated.

A comparison of coseismic landslide inventories indicates that blind rupture-earthquakes induced fewer landslides than surface rupture-earthquakes on thrust or reverse faults. The location, abundance, and area affected by coseismic landslides are linked with first order to the type and daylighting of rupture, local topographic relief, and earthquake magnitude. The frequency-size distribution and total area of landslides triggered by the 2010 Haiti earthquake is below those of similar magnitude events, mainly because of the lower static stress drop and mean fault displacement during a blind rupture.

Please cite this article as: Gorum, T., et al., Complex rupture mechanism and topography control symmetry of mass-wasting pattern, 2010 Haiti earthquake, Geomorphology (2012), http://dx.doi.org/10.1016/j.geomorph.2012.11.027

The directivity of rupture propagation amplified local topographic differences that superpose the symmetric pattern of the coseismic landslides. Our results provide a testable hypothesis for further quantifying the effects of the surface or blind rupture-earthquakes on coseismic landsliding. Thus, research on coseismic landslides needs a larger number of complete inventories together with more comprehensive study of earthquake-triggered landslides in the future.

Acknowledgements

This research was supported by the United Nations University – ITC Center for Spatial Analysis for Disaster Risk Management (www.itc.nl/unu-drm). O. Korup acknowledges support by the Potsdam Research Cluster for Georisk Analysis, Environmental Change and Sustainability (PROGRESS). We are grateful to Gavin P. Hayes and Eric J. Fielding for generously providing the field based coral uplift measurements and the InSAR-derived surface-deformation data. We thank Alexander Strom and an anonymous referee for their constructive and helpful comments on an earlier version of this paper.

Appendix A. Supplementary material

Supplementary data associated with this article can be found in the online version, at http://dx.doi.org/10.1016/j.geomorph.2012.11.027. These data include Google maps of the most important areas described in this article.

References

Abrahamson, N.A., Silva, W.J., 1997. Empirical response spectral attenuation relations for shallow crustal earthquakes. Seismological Research Letters 68, 94–127.

Abrahamson, N.A., Silva, W.J., 2008. Summary of the Abrahamson & Silva NGA groundmotion relations. Earthquake Spectra 24, 67–97.

Abrahamson, N.A., Somerville, P.C., 1996. Effects of the hanging wall and footwall on ground motions recorded during the Northridge Earthquake. Bulletin of the Seismological Society of America 86, 93–99.

Alfaro, P., Delgado, J., García-Tortosa, F.J., Lenti, L., López, J.A., López-Casado, C., Martino, S., 2012. Widespread landslides induced by the Mw 5.1 earthquake of 11 May 2011 in Lorca, SE Spain. Engineering Geology 137–138, 40–52.

Anderson, J.G., 2003. Strong-motion seismology. In: William, H.K.L., Kanamori, H., Jennings, P.C., Kisslinger, C. (Eds.), International Handbook of Earthquake and Engineering Seismology (Part B), vol. 81. Academic Press, pp. 937–965.

Bakun, W.H., Flores, C.H., ten Brink, U.S., 2012. Significant earthquakes on the Enriquillo Fault System, Hispaniola, 1500–2010: implications for seismic hazard. Bulletin of the Seismological Society of America 102, 18–30.

Bird, M.I., Longstaffe, F.J., Fyfe, W.S., Bildgen, P., 1992. Oxygen-isotope systematics in a multiphase weathering system in Haiti. Geochimica Et Cosmochimica Acta 56, 2831–2838.

Bonilla, M.G., 1988. Minimum earthquake magnitude associated with coseismic surface faulting. Bulletin of the International Association of Engineering Geology 25, 17–29.

Calais, E., Freed, A., Mattioli, G., Amelung, F., Jónsson, S., Jansma, P., Hong, S.-H., Dixon, T., Prépetit, C., Momplaisir, R., 2010. Transpressional rupture of an unmapped fault during the 2010, Haiti earthquake. Nature Geoscience 3, 794–799.

Campbell, K.W., 1981. Near-source attenuation of peak horizontal acceleration. Bulletin of the Seismological Society of America 71, 2039–2070.

Campbell, K.W., 2003. Strong-motion attenuation relations. In: William, H.K.L., Kanamori, H., Jennings, P.C., Kisslinger, C. (Eds.), International Handbook of Earthquake and Engineering Seismology (Part B), vol. 81. Academic Press, New York, pp. 1003–1012.

Cavallo, E.A., Powell, A., Becerra, O., 2010. Estimating the direct economic damage of the earthquake in Haiti. IDB Working Paper Series 163 . (16 pp.).

Chen, J., Helmberger, D.V., Wald, D.J., Ma, K.F., 2003. Slip history and dynamic implications of the 1999 Chi-Chi, Taiwan, earthquake. Journal of Geophysical Research 108 (B9), 2412. http://dx.doi.org/10.1029/2002JB001764.

Escuder-Viruete, J., Perez-Estaun, A., Contreras, F., Joubert, M., Weis, D., Ullrich, T.D., Spadea, P., 2007. Plume mantle source heterogeneity through time: Insights from the Duarte Complex, Hispaniola, northeastern Caribbean. Journal of Geophysical Research 112 (B4), B04203. http://dx.doi.org/10.1029/2006JB004323.

Faccioli, E., Vanini, M., Frassine, L., 2002. Complex site effects in earthquake ground motion, including topography. 12th European Conference on Earthquake Engineering 9–13 September 2002. Barbican Centre, London, UK (Paper Reference 844, 22 pp.).

Fan, X., van Westen, C.J., Korup, O., Gorum, T., Xu, Q., Dai, F.C., Huang, R.Q., Wang, G., 2012a. Transient water and sediment storage of the decaying landslide dams induced by the 2008 Wenchuan earthquake, China. Geomorphology 171–172, 58–68.

Fan, X., van Westen, C.J., Xu, Q., Gorum, T., Dai, F.C., 2012b. Analysis of landslide dams induced by the 2008 Wenchuan earthquake. Journal of Asian Earth Sciences 57, 25–37.

Fiorucci, F., Cardinali, M., Carlà, R., Rossi, M., Mondini, A.C., Santurri, L., Ardizzone, F., Guzzetti, F., 2011. Seasonal landslide mapping and estimation of landslide mobilization rates using aerial and satellite images. Geomorphology 129, 59–70.

U.S. Geological Survey, 2010. Landslide Photo Collections, Haiti Earthquake-Induced Landslides, January 12, 2010. http://landslides.usgs.gov/learning/photos/international/haiti_earthquake-induced_landslides__january_12__2010.

Gorum, T., Fan, X., van Westen, C.J., Huang, R., Xu, Q., Tang, C., Wang, G., 2011. Distribution pattern of earthquake-induced landslides triggered by the 12 May 2008 Wenchuan earthquake. Geomorphology 133, 152–167.

Harp, E.L., Jibson, R.W., 1995. Inventory of landslides triggered by the 1994 Northridge, California earthquake. US Geol. Surv. Open-File Rep. 95–213 (17 pp.).

Harris, R.A., 1998. Introduction to special section: stress triggers, stress shadows, and implications for seismic hazard. Journal of Geophysical Research 103, 24347–24358.

Hashimoto, M., Fukushima, Y., Fukahata, Y., 2011. Fan-delta uplift and mountain subsidence during the Haiti 2010 earthquake. Nature Geoscience 4, 255–259.

Hayes, G.P., Briggs, R.W., Sladen, A., Fielding, E.J., Prentice, C., Hudnut, K., Mann, P., Taylor, F.W., Crone, A.J., Gold, R., Ito, T., Simons, M., 2010. Complex rupture during the 12 January 2010 Haiti earthquake. Nature Geoscience 3, 800–805.

Hough, S.E., Altidor, J.R., Anglade, D., Given, D., Janvier, M.G., Maharrey, J.Z., Meremonte, M., Mildor, B.S., Prepetit, C., Yong, A., 2010. Localized damage caused by topographic amplification during the 2010 M 7.0 Haiti earthquake. Nature Geoscience 3, 778–782.

Iwahashi, J., Watanabe, S., Furuya, T., 2001. Landform analysis of slope movements using DEM in Higashikubiki area, Japan. Computers & Geosciences 27, 851–865.

Iwahashi, J., Watanabe, S., Furuya, T., 2003. Mean slope-angle frequency distribution and size frequency distribution of landslide masses in Higashikubiki area, Japan. Geomorphology 50, 349–364. http://dx.doi.org/10.1016/S0169-555X(02)00222-2.

Jenness, J., 2006. Topographic Position Index (tpi_jen.avx) extension for ArcView 3.x, v. 1.2. Jenness Enterprises . (Available at: http://www.jennessent.com/arcview/tpi.htm).

Jibson, R.W., Harp, E.L., 2011. Field reconnaissance report of landslides triggered by the January 12, 2010, Haiti earthquake. U.S. Geological Survey Open-File Report 2011–1023. (19 pp.).

Keefer, D.K., 1984. Landslides caused by earthquakes. Geological Society of America Bulletin 95, 406–421.

King, G.C.P., Stein, R.S., Lin, J., 1994. Static stress changes and the triggering of earthquakes. Bulletin of the Seismological Society of America 84, 935–953.

Korup, O., 2004. Geomorphic implications of fault zone weakening: slope instability along the Alpine Fault, South Westland to Fiordland. New Zealand Journal of Geology and Geophysics 47, 257–267.

Korup, O., 2008. Rock type leaves topographic signature in landslide-dominated mountain ranges. Geophysical Research Letters 35, L11402. http://dx.doi.org/10.1029/2008GL034157.

Korup, O., Schlunegger, F., 2009. Rock-type control on erosion-induced uplift, eastern Swiss Alps. Earth and Planetary Science Letters 278, 278–285. http://dx.doi.org/10.1016/j.epsl.2008.12.012.

Korup, O., Weidinger, J.T., 2011. Rock type, precipitation, and the steepness of Himalayan threshold hillslopes. In: Gloaguen, R., Ratschbacher, L. (Eds.), Growth and collapse of the Tibetan Plateau: Geological Society of London Special Publications, 353, pp. 235–249.

Lambert, M.L, Gaudin, J. and Cohen, R., 1987. Carte Geologique D'Haiti, Feuille Sud-Est: Port-au-Prince, 1:250,000, IMAGEO-CNRS.

Liao, H.W., Lee, C.T., 2000. Landsides triggered by the Chi-Chi Earthquake. Proceedings of the 21st Asian Conference on Remote Sensing, Taipei, volume 1–2, pp. 383–388.

Liu-Zeng, J., Zhang, Z., Wen, L., Tapponnier, P., Sun, J., Xing, X., Hu, G., Xu, Q., Zeng, L., Ding, L., Ji, C., Hudnut, K.W., van der Woerd, J., 2009. Co-seismic ruptures of the 12 May 2008, Ms 8.0 Wenchuan earthquake, Sichuan: east–west crustal shortening on oblique, parallel thrusts along the eastern edge of Tibet. Earth and Planetary Science Letters 286, 355–370.

Manaker, D.M., Calais, E., Freed, A.M., Ali, S.T., Przybylski, P., Mattioli, G., Jansma, P., Prépetit, C., de Chabalier, J.B., 2008. Interseismic plate coupling and strain partitioning in the northeastern Caribbean. Geophysical Journal International 174, 889–903.

Mann, P., Matumoto, T., Burke, K., 1984. Neotectonics of Hispaniola-plate motion, sedimentation, and seismicity at a restraining bend. Earth and Planetary Science Letters 70, 311–324.

Mann, P., Taylor, F.W., Edwards, R.L., Ku, T.L., 1995. Actively evolving microplate formation by oblique collision and sideways motion along strike-slip faults: an example from the northwestern Caribbean plate margin. Tectonophysics 246, 1–69.

Martinez-Diaz, J.J., Bejar-Pizarro, M., Alvarez-Gomez, J.A., Mancilla, F.D., Stich, D., Herrera, G., Morales, J., 2012. Tectonic and seismic implications of an intersegment rupture the damaging May 11th 2011 Mw 5.2 Lorca, Spain, earthquake. Tectonophysics 546, 28–37.

McCalpin, J.P., 2009. Paleoseismology, 2nd edition. Academic Press, New York. 629 pp.

Mercier de Lépinay, B., Deschamps, A., Klingelhoefer, F., Mazabraud, Y., Delouis, B., Clouard, V., Hello, Y., Crozon, J., Marcaillou, B., Graindorge, D., Vallée, M., Perrot, J., Bouin, M.P., Saurel, J.M., Charvis, P., St-Louis, M., 2011. The 2010 Haiti earthquake: a complex fault pattern constrained by seismologic and tectonic observations. Geophysical Research Letters 38, L22305. http://dx.doi.org/10.1029/2011GL049799.

Meunier, P., Hovius, N., Haines, A.J., 2008. Topographic site effects and the location of earthquake induced landslides. Earth and Planetary Science Letters 275, 221–232.

Molnar, P., Anderson, R.S., Anderson, S.P., 2007. Tectonics, fracturing of rock, and erosion. Journal of Geophysical Research 112, F03014. http://dx.doi.org/10.1029/2005JF000433.

NOAA (National Oceanic, Atmorspheric Administration), 2012. National Oceanographic Data Library, Haiti Climatological Data. http://docs.lib.noaa.gov/rescue/data_rescue_haiti.html.

Oglesby, D.D., Archuleta, R.J., Nielsen, S.B., 1998. Earthquakes on dipping faults: the effects of broken symmetry. Science 280, 1055–1059.

Oglesby, D.D., Archuleta, R.J., Nielsen, S.B., 2000. The three dimensional dynamics of dipping faults. Bulletin of the Seismological Society of America 90, 616–628.

Ohta, Y., Ohzono, M., Miura, S., Iinuma, T., Tachibana, K., Takatsuka, K., Miyao, K., Sato, T., Umino, N., 2008. Coseismic fault model of the 2008 Iwate-Miyagi Nairiku earthquake deduced by a dense GPS network. Earth Planets Space 60, 1197–1201.

Paolucci, R., 2002. Amplification of earthquake ground motion by steep topographic irregularities. Earthquake Engineering and Structural Dynamics 31, 1831–1853.

Prentice, C.S., Mann, P., Crone, A.J., Gold, R.D., Hudnut, K.W., Briggs, R.W., Koehler, R.D., Jean, P., 2010. Seismic hazard of the Enriquillo-Plantain Garden fault in Haiti inferred from palaeoseismology. Nature Geoscience 3, 789–793.

Sappington, J.M., Longshore, K.M., Thompson, D.B., 2007. Quantifying landscape ruggedness for animal habitat analysis: a case study using bighorn sheep in the Mojave Desert. The Journal of Wildlife Management 71, 1419–1426.

Sen, G., Hickeyvargas, R., Waggoner, D.G., Maurrasse, F., 1988. Geochemistry of basalts from the Dumisseau formation, southern Haiti — implications for the origin of the Caribbean Sea crust. Earth and Planetary Science Letters 87, 423–437.

Shafique, M., van der Meijde, M., Kerle, N., van der Meer, F.D., 2011. Impact of DEM source and resolution on topographic seismic amplification. International Journal of Applied Earth Observation and Geoinformation 13, 420–427.

Shen, Z.K., Ge, B.X., Jackson, D.D., Potter, D., Cline, M., Sung, L.Y., 1996. Northridge earthquake rupture models based on the global positioning system measurements. Bulletin of the Seismological Society of America 86, 37–48.

Somerville, P.G., 2000. New developments in seismic hazard estimation. Proc., 6th International Conference on Seismic Zonation, Nov. 12–15, 2000, Palm Springs, CA, Proc. CD-ROM. Earthquake Engineering Research Institute, Oakland, CA (25 pp.).

Somerville, P.G., Pitarka, A., 2006. Differences in earthquake source and ground motion characteristics between surface and buried earthquakes. Processing of 8th National Conference on Earthquake Engineering, Paper No. 977.

Stein, R.S., 1999. The role of stress transfer in earthquake occurrence. Nature 402, 605–609.

van Westen, C.J., Castellanos Abella, E.A., Sekhar, L.K., 2008. Spatial data for landslide susceptibility, hazards and vulnerability assessment: an overview. Engineering Geology 102, 112–131.

van Zuidam, R.A., 1985. Aerial Photo-Interpretation in Terrain Analysis and Geomorphologic Mapping. ITC. Smits Publishers, The Hague, Netherlands.

Wells, D.L., Coppersmith, K.J., 1994. Empirical relationships among magnitude, rupture length, rupture area, and surface displacement. Bulletin of the Seismological Society of America 84, 974–1002.

Wolinsky, M.A., Pratson, L.F., 2005. Constraints on landscape evolution from slope histograms. Geology 33, 477–480.

Yagi, H., Sato, G., Higaki, D., Yamamoto, M., Yamasaki, T., 2009. Distribution and characteristics of landslides induced by the Iwate-Miyagi Nairiku Earthquake in 2008 in Tohoku District, Northeast Japan. Landslides 6, 335–344.

Please cite this article as: Gorum, T., et al., Complex rupture mechanism and topography control symmetry of mass-wasting pattern, 2010 Haiti earthquake, Geomorphology (2012), http://dx.doi.org/10.1016/j.geomorph.2012.11.027